KeAi
CHINESE ROOTS
GLOBAL IMPACT

Available online at www.keaipublishing.com/en/journals/journal-of-magnesium-and-alloys/

ScienceDirect

Journal of Magnesium and Alloys 12 (2024) 4976–4987

www.elsevier.com/locate/jma

Full Length Article

Grain growth stagnation at 525 °C by nanoparticles in a solid-state additively manufactured Mg-4Y-3RE alloy

Xingjian Zhao[a], Daniel Olden[a], Brady Williams[b], Abhishek Pariyar[a], Dalong Zhang[b], Matthew Murphy[c], Philippa Reed[a], Paul Allison[b], Brian Jordon[b], Jiahui Qi[d], W. Mark Rainforth[d], Dikai Guan[a,*]

[a] *Department of Mechanical Engineering, University of Southampton, Southampton, SO17 1BJ, United Kingdom*
[b] *Point-of-Need Innovations (PONI) Center, Baylor University, Waco, 76704, United States*
[c] *Luxfer MEL Technologies, Elektron Technology Centre, Lumns Lane, Manchester M27 8LN, United Kingdom*
[d] *School of Chemical, Materials and Biological Engineering, The University of Sheffield, Sheffield, S1 3JD, United Kingdom*

Received 5 October 2024; received in revised form 29 November 2024; accepted 5 December 2024
Available online 20 December 2024

Abstract

Ultrafine-grained (UFG) materials exhibit high strengths due to grain boundary strengthening, but grains can grow rapidly if post heat treatment is required, making it challenging to achieve grain boundary and precipitation strengthening simultaneously. Grain growth stagnation at 525 °C (0.87 T_m, melting point) was observed in a Mg-4Y-3RE alloy fabricated by additive friction stir deposition (AFSD), a novel solid-state additive manufacturing technology. The AFSD processing produced a UFG microstructure and two major second phases, $Mg_{41}RE_5$ and nanoparticles containing Y and O. After solid solution treatment (SST) at 525 °C for 72 h, no noticeable grain growth occurred. While $Mg_{41}RE_5$ particles dissolved into the matrix within 4 h of SST, the nanoparticles remained stable and unaltered. The observed grain growth stagnation is attributed to Zener pinning by these thermally stable nanoparticles. These new findings offer a novel approach to designing UFG materials with exceptional thermal stability for high-temperature applications.

Keywords: Grain growth; Magnesium alloys; Ultrafine grained microstructure; Nanoparticles; Additive friction stir deposition.

1. Introduction

According to the classical Hall-Petch or grain-boundary strengthening theory, grain refinement has been widely recognised to be an effective route to improve the strength of metals and alloys. Materials with an average grain size ranging from ~100 nm up to ~1 μm are referred to as ultrafine-grained (UFG) alloys [1]. UFG materials with improved strengths have been successfully achieved in several important alloying systems, including steels [2], Cu alloys [1], Al alloys [3], Mg alloys [4,5], etc. There are several approaches to achieve the UFG structure in metallic materials. Several severe plastic deformation (SPD) techniques [6,7], including high pressure torsion (HPT) [8,9], equal channel angular pressing (ECAP) [10], accumulative roll bonding (ARB) [11], and friction stir processing (FSP) [12,13], have been widely used for the fabrication of UFG materials. Powder metallurgy methods [14] also play a fundamental role in the production of UFG materials. Although UFG alloys can be produced by various techniques, preserving the UFG structure is challenging, if the alloys need to undergo elevated temperature solid solution treatment (SST) followed by ageing (T6) for the maximisation of precipitation hardening. The refined grain structure, compared to the coarse grain structure, is prone to undergo rapid grain growth at elevated temperatures [15], leading to a "trade-off" between precipitation hardening and grain boundary strengthening.

* Corresponding author.
E-mail address: dikai.guan@soton.ac.uk (D. Guan).

https://doi.org/10.1016/j.jma.2024.12.010

Efforts have been made to inhibit or retard the grain growth in UFG alloys at elevated temperatures and achievements have been made in several alloy systems. Bai et al. [16] prepared a heat-resistant UFG oxide-dispersion-strengthened (ODS) Al alloy by powder metallurgy. The average grain size only slightly increased from 220 nm to 228 nm after being kept at 600 °C (0.93 Tm, Tm is the melting point) for 8 h. Croteau et al. [3] consolidated an UFG Al-Mg-Zr alloy by shear-assisted processing and extrusion (ShAPE). The average grain size increased from about 0.9 μm to about 1.4 μm after ageing at 400 °C for 120 h. Liang et al. [1] fabricated an UFG Cu alloy with minor addition of Co by rolling. The average grain size remained around 3.5 μm after annealing at 750 °C (0.75 Tm) for 1 hour. Despite the progress made in Al alloys, Cu alloys and other alloy systems, achieving highly thermal stability in UFG Mg alloys has remained intractable. Stráská et al. [5] produced an UFG AZ31B Mg alloy with an average grain size of 0.94 μm by combining extrusion and equal channel angular pressing (EX-ECAP). The average grain size remained around 1 μm at 190 °C 1 h, but rapidly increased to about 10 μm when the temperature reached 450 °C. Fekete et al. [17] obtained an UFG Mg97.94Zn0.56Y1.5 alloy by consolidating rapidly solidified ribbons. The average grain size was around 790 nm and remained below 1 μm after annealing at 400 °C for 24 h. Even in rare earth or silver containing Mg alloys (e.g. WE43, WE54, QE22), which are designated mainly for high temperature purposes, grain growth is still evident at high temperatures. Minárik et al. [18] fabricated an UFG WE43 alloy with an average grain size of about 340 nm by ECAP. The grain size remained stable up to 280 °C for 1 hour, yet grains rapidly grew over 20 μm in 1 hour when the temperature was raised to 460 °C. To the best of our knowledge, the UFG microstructure has not been successfully retained in Mg alloys at elevated SST temperatures.

In this work, a Mg-4Y-3RE (Elektron 43) alloy component was built by additive friction stir processing (AFSD) [19,20], an emerging solid-state additive manufacturing technology. Compared to conventional fusion-based additive manufacturing technologies such as laser powder bed-fusion (LPBF) and direct energy deposition (DED), AFSD can produce fully dense pore-free components without hot cracks [21]. AFSD has been successfully used to deposit several metals and alloys, including stainless steels [22,23], Cu alloys [24], Al alloys [25,26], and Mg alloys [27–31]. A UFG structure was achieved in the AFSDed component and we found the grain growth of ultrafine grains in the as-deposited Mg alloy was fully restricted, showing negligible grain growth (from 1.05±0.49 μm to 1.06±0.48 μm) and exceptional thermal stability after solid solution treatment at 525 °C (0.87 T_m, melting point of Elektron 43) for 72 h. The early stage of this abnormal phenomenon was systematically investigated using various microstructure characterisation techniques, and the findings in this work could shed light on designing new high strength UFG Mg alloys for industry applications, especially in the emerging research area of solid-state additive manufacturing.

Table 1
Chemical composition (weight %) of Elektron 43 Mg alloy.

Element	Y	Rare Earths	Zr	Mg
Weight percent (wt %)	3.7–4.3	2.3–3.5	Minimum 0.2	Balance

2. Material and methods

2.1. Feedstock material and AFSD set-up

The feedstock material for AFSD was Elektron 43 Mg alloy extruded bars produced by Luxfer MEL Technologies. The chemical composition of the material is shown below in Table 1. The feedstock has a square cross-section with a side length of 9.5 mm. The AFSD process was performed on a commercially available MELD B8 machine. The tool for AFSD is made of H13 steel. It has a cylindrical shape with a square hollow channel embedded at the centre which is compatible with the feedstock. The bottom surface of the tool also has a 'teardrop' structure [27]. In the beginning, the distance between the tool and the substrate surface was kept constant at 1 mm to control the deposition layer thickness. After the completion of one layer, the tool was lift up for another 1 mm and travel along the opposite direction to deposit the next layer. The rotational speed, feeding rate and traverse speed were 325 RPM, 63.5 mm/min, and 152.4 mm/min, respectively. No protection gas or extra cooling system was used during the printing process. More details of the AFSD set-up can be found in a separate published work [27].

2.2. Post heat treatment

To investigate the microstructure evolution in the AFSDed Elektron 43 at an elevated temperature, samples machined from the as-deposited build were held at 525 °C for 4 h, 24 h and 72 h in a box furnace followed by water quenching to maintain the microstructure after keeping at 525 °C. An extruded feedstock sample was also treated at the same temperature for 0.5 h, 1 h, and 2 h for comparison.

2.3. Microstructure characterisation

Samples for scanning electron microscopy (SEM) and electron backscattered diffraction (EBSD) were prepared by mechanical grinding and polishing. Samples were firstly ground by silicon carbide grinding papers and then polished by 1 μm, 0.25 μm alcohol-based diamond suspension. The final polishing was done by 40 nm colloidal silica suspension. SEM and EBSD were operated on a JEOL JSM-7200F SEM equipped with an Oxford Instrument C–Nano EBSD detector. The accelerating voltage for SEM image acquirement and EBSD scanning was both at 20 kV. The step size of EBSD scanning chosen 0.1 μm for all the AFSDed samples, 0.25 μm for the feedstock, and 1 um for the SSTed feedstock. EBSD data were collected and analysed by the Aztec Crystal software.

Samples for transmission electron microscopy (TEM) were first mechanically thinned and then polished using twin jet

polishing method. TEM images and energy dispersive X-ray spectroscopy (EDS) scans were taken on an FEI Talos F200X microscope equipped with a Super-X G2 EDS detector, operated at 200 kV. TEM images and EDS data were analysed by ImageJ and Velox, respectively.

2.4. Hardness tests

Hardness data was collected by a Zwick FM-300 hardness tester using Vickers hardness mode. The load for all samples was set to 200 g, and the dwell time was 15 s. At least 16 indentations were taken to minimise the uncertainty from possible microstructural heterogeneity. Since this work focuses on the exceptional thermal stability, the hardness test results will not be elaborated and will be reported in another work.

3. Results

3.1. Grain size evolution

Grain size evolution of the AFSD and the feedstock samples are provided in Fig. 1a–d and e–h, respectively. The average grain size of the AFSDed sample was measured to be 1.05±0.49 μm based on the EBSD IPF map in Fig. 1a, indicating a UFG structure was obtained by simply carrying out the AFSD without further processing or treatment. The UFG structure remained unchanged after 4h-SST at 525 °C, measured 1.03±0.47 μm, as shown in Fig. 1b. The grain size even remained unchanged after 24h-SST and 72h-SST at 525 °C as shown in Fig. 1c–d, measured 1.05±0.47 μm and 1.06±0.48 μm, respectively. In contrast, the average grain size in the feedstock material was measured to be 2.64±1.27 μm, but quickly grew to 32.0 ± 17.3 μm, 42.0 ± 22.1 μm, and 56.5 ± 30.3 μm after being kept at the same temperature for 0.5 h, 1 h, and 2 h, respectively, as shown in Fig. 1e–h.

3.2. Second phase evolution

Fig. 2 shows the second phase evolution in the AFSDed and feedstock sample before and after SST. For the AFSDed sample, the fraction of second phases significantly decreased, as shown in the typical SEM-BSE images (Fig. 2a,d). As shown in the high angle annular dark field (HAADF) images and corresponding bright field (BF) images(Fig. 2b,c,e,f), the AFSDed sample contains polygonal second phase particles with a size ranging from hundreds of nanometres to a few micrometres distributed along the grain boundaries. There are also dense fine particles distributed across the entire sample surface. These nanoparticles were distributed at grain boundaries, triple junctions, and within grains, yet the particle density was slightly lower in the grain interior. After 4h-SST, those large polygonal second phase particles could no longer be observed, whilst for those nanoparticles, the fraction, size, and distribution remained approximately unchanged (Fig. 2e). In addition, a few particles with round or tetragonal shape were also observed. For the feedstock sample, there were fine second phases along grain boundaries and large second phases linearly distributed along the extrusion direction (Fig. 2g). After 2h-SST, second phases along grain boundaries fully dissolved into the matrix, whilst linearly distributed round and tetragonal shape particles (Fig. 2h). These residual second phases in both samples are believed to be common inclusions such as rare earth hydrides (e.g. REH_2) and oxides [10,27,32].

Table 2
EDS Chemical composition (atomic %) for regions detailed in Fig. 3.

	Mg	Y	Nd	Gd	Zr	O
Site A (particle)	76.4%	8.1%	1.3%	0.5%	1.4%	14.1%
Site B (matrix)	90.1%	0.6%	0.2%	0.1%	0.3%	8.7%
Site C (particle)	79.2%	7.9%	0.8%	0.3%	0.7%	11.1%
Site D (particle)	77.9%	9.1%	1.2%	0.4%	1.5%	10.0%
Site E (matrix)	93.5%	0.7%	0.3%	0.1%	0.2%	5.2%

The TEM-EDS results of the AFSDed and AFSDed-4h-SST samples in Fig. 3 reveal the chemical composition of the second phases. EDS maps in Fig. 3a show that the large polygonal second phase are rich in RE elements of Nd and Gd. Further selective area electron diffraction (SAED) pattern of the second phase particle was obtained. The measurement of interplanar spacing and angles confirms it has a $Mg_{41}RE_5$ structure (tetragonal crystal structure, $a = b = 14.74$ Å and $c = 10.40$ Å [33]). EDS maps in Fig. 3b and c suggest that the nanoparticles in both AFSDed and AFSDed-4h-SST samples are mainly rich in Y and O, though Nd, Gd, Zr, were also detected. It needs to be noted that the EDS maps here do not reveal the quantitative concentration of the elements. The element concentration of nanoparticles and matrix were collected from selected points (Points A-E marked by red arrows in Fig. 3) and shown in Table 2. Samples before and after the SST show a similar chemical composition in matrix and nanoparticles. In the Mg matrix region of both samples, all the alloying elements show a concentration below 1 at%. O was also detected, which is believed to come from the sample surface oxidation. In the nanoparticle regions, the concentration of Nd, Gd, Zr is slightly higher than that in the matrix. The concentration of Y is one order of magnitude higher than that in the matrix, reaching nearly 10 at%. The concentration of O is also higher in the nanoparticles, reaching over 10 at%. The atomic fraction between Y to O is close to 2:3, indicating these nanoparticles are highly likely to be Y_2O_3, yet further characterisation needs to be done for validation. The Mg signal in the EDS spectra from these nanoparticles is attributed to the interaction volume of electron beam being larger than the nanoparticles and therefore including signals from adjacent matrix regions. The detailed phase identification and analysis of these uncommon oxygen-enriched particles will be systematically analysed in our future work.

Fig. 4a,b shows a more detailed structure of the nanoparticles and the interaction between nanoparticles and grain boundaries. Some of the nanoparticles were agglomerations of many finer particles instead of a single crystal. The single particles usually have a circular or elliptical shape, and the

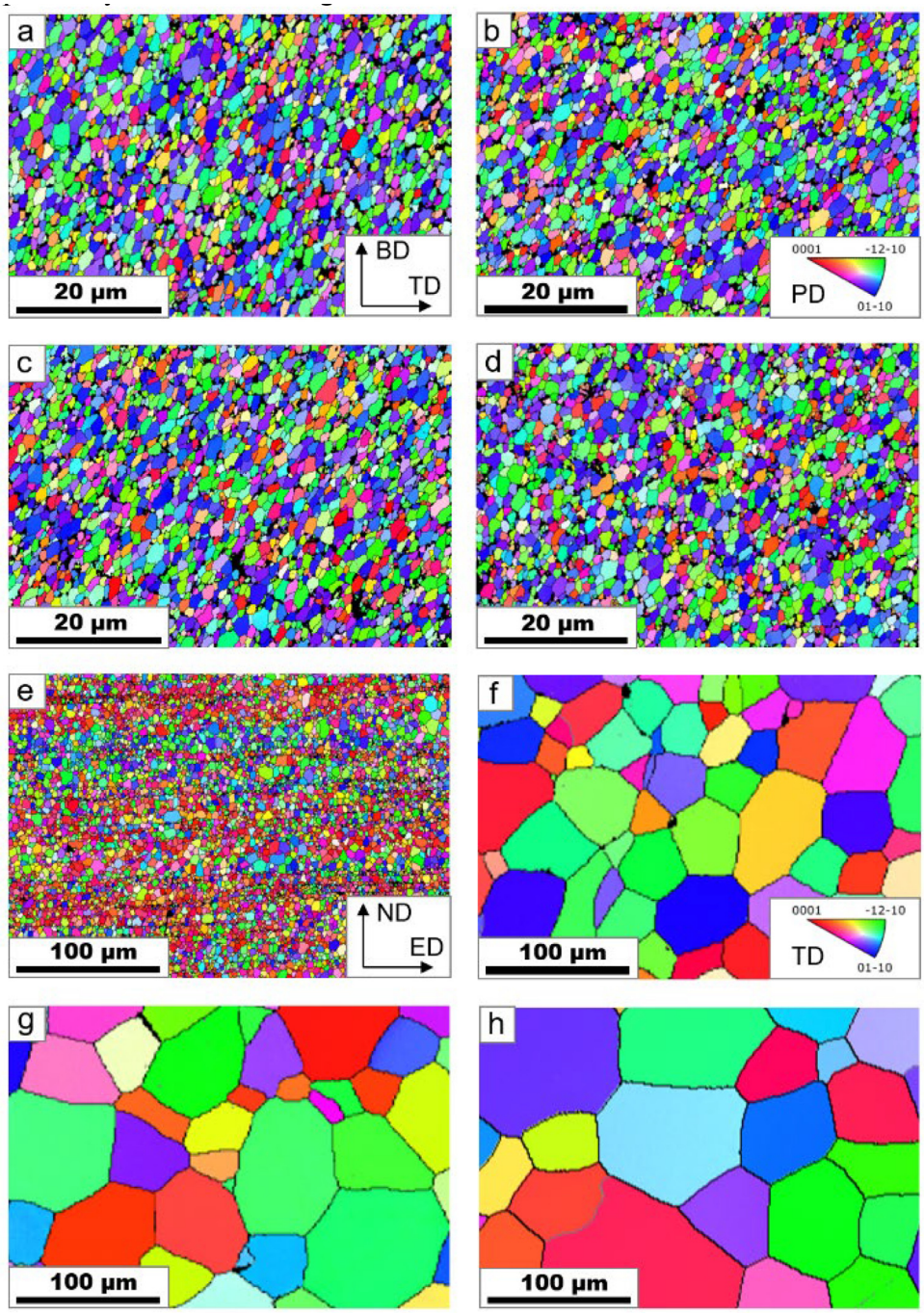

Fig. 1. EBSD IPF maps of AFSDed samples after SST for (a) 0 h, (b) 4 h, (c) 24 h, (d) 72 h, under × 2000 magnification. BD is the building direction, TD is the transverse direction, PD is the processing direction (longitudinal direction); and extruded feedstock samples after SST for (e) 0 h, (f) 0.5 h, (g) 1 h, (h) 2 h, under × 400 magnification. ED is the extrusion direction, ND is the normal direction, TD is the transverse direction.

size mostly ranges from 5 to 20 nm. The agglomerated particles have irregular shapes, and the size ranges from tens to hundreds of nanometres. This explains why there was a slight increase of Nd, Gd, and Zr concentration in the nanoparticle region, as alloying elements would segregate at boundaries in the agglomerated particles. These nanoparticles interacted strongly with grain boundaries and triple junctions, and key information is marked for illustration, as shown in Fig. 4c. Interestingly, the grain boundary between G3 and G4, which is free of nanoparticles, is relatively straight. Whilst there is significant change of grain boundary curvature (i.e. grain boundary bowing) around the nanoparticles, such as the grain boundaries between G1-G2, and G1-G3. At the triple junction TJ1 where is free of nanoparticles, the angles are around 120°, whilst at TJ2 where nanoparticles present, the angles are not close to 120°. Such interaction was commonly observed in other regions in the sample, as shown in Fig. 4d–f, indicated by red arrows.

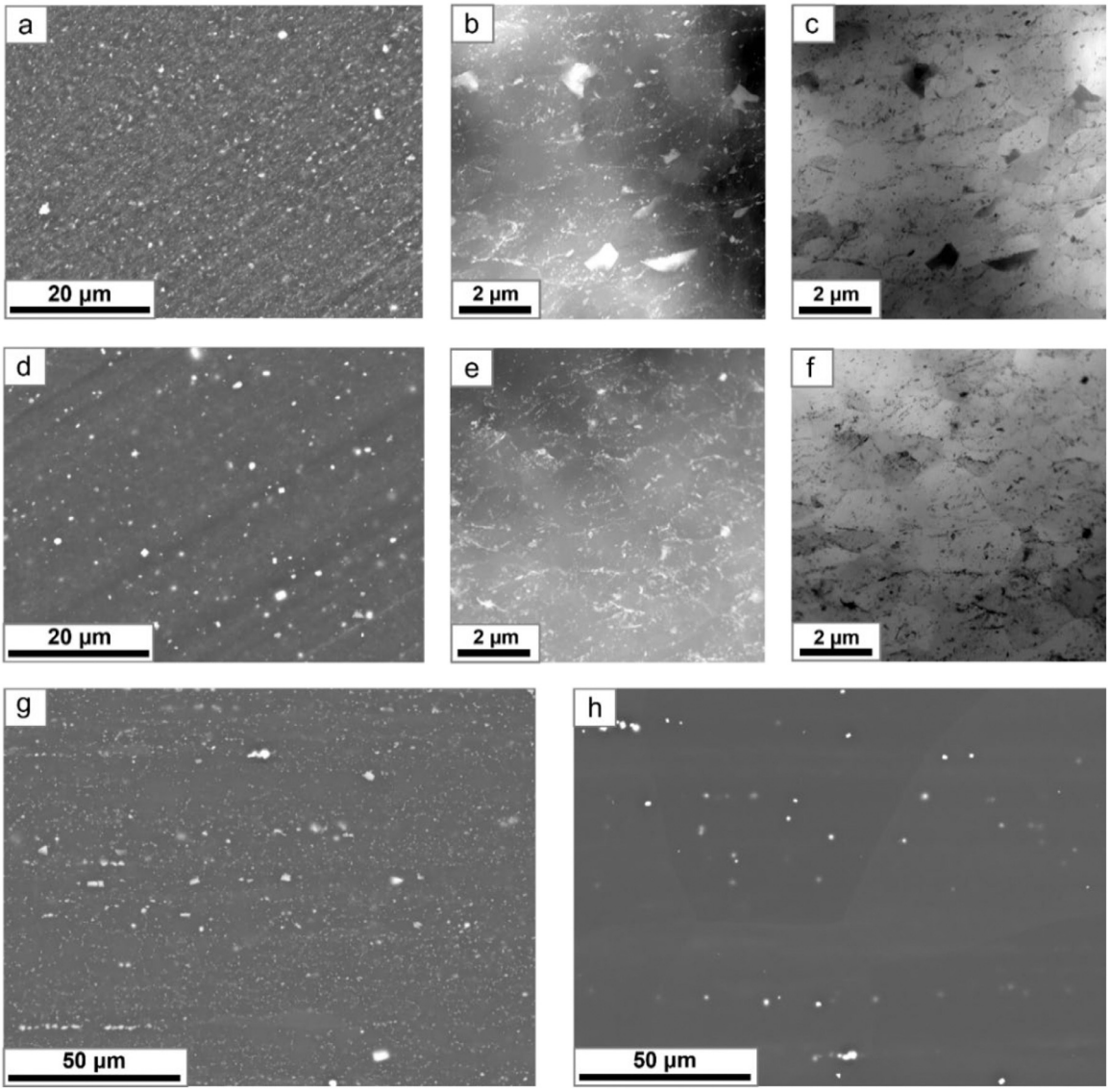

Fig. 2. AFSDed sample (a) SEM-BSE image, (b) HAADF image, (c) BF image; AFSDed-4h-SST sample (d) SEM-BSE image, (e) HAADF image, (f) BF image; SEM-BSE images of feedstock sample (g) 0h-SST, (h) 2h-SST.

3.3. Hardness test results

The hardness test results are shown in Fig. 5. The AFSDed sample shows a hardness of 88.6 ± 2.3 HV. It is nearly comparable to that of commercially extruded products after T5 treatment, which have a hardness value of 90.2 ± 5.0 HV. After 4h-SST, the hardness value dropped by ~5 to 83.6 ± 3.5 HV. Nevertheless, the AFSDed-4h-SST sample still shows a higher hardness compared to the feedstock material which has a hardness about 78.1 ± 1.3 HV. This reduction in hardness is attributed to the ineffectiveness of precipitation strengthening during heat treatment due to precipitate redissolution. Further optimisation of the heat treatment, high-temperature hardness tests, and related mechanical strength will be reported in another work as mentioned before. Nevertheless, these additional considerations will not alter the primary conclusions of this study, which centres on illustrating the grain growth stagnation behaviour at solid solution treatment temperatures, which has never been reported in Mg alloys before.

4. Discussion

4.1. Grain growth rate

The change of grain size with temperature is plotted in Fig. 6a. Rapid grain growth was observed in the Elektron 43 feedstock sample, with the grain size increasing by over 21 times after being held at 525 °C for 2 h (see Fig. 1e–f). Such rapid grain coarsening at elevated temperatures in Mg-4Y-3RE has also been widely reported by other researchers [32,34, 35]. However, there was no statistically meaningful grain growth in the AFSDed material. To quantitatively evaluate the difference in grain growth behaviour between the feedstock and the AFSDed material, the following equation

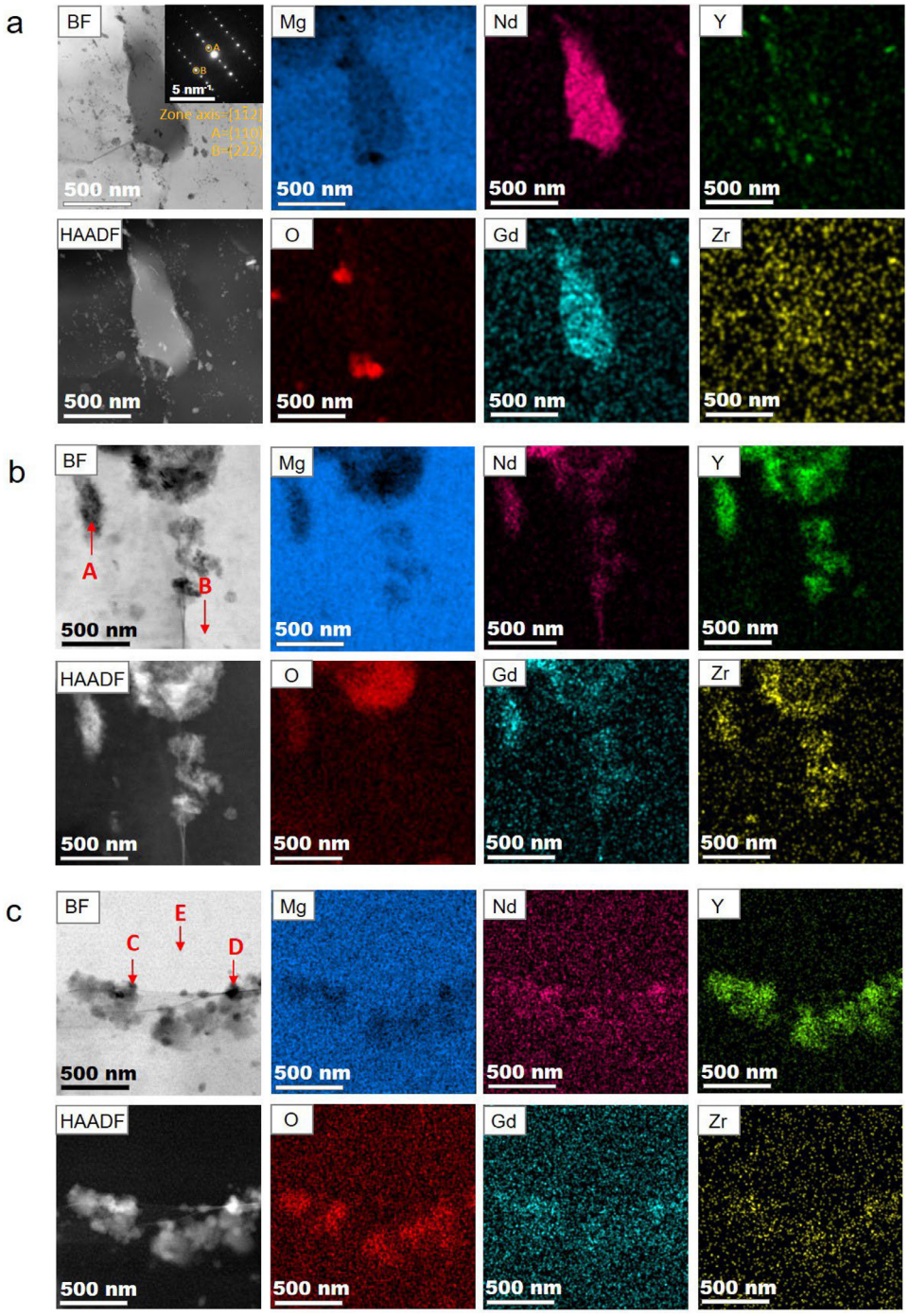

Fig. 3. BF images, HAADF images, and EDS maps of (a) a large second phase particle and (b) nanoparticles in AFSDed sample, and (c) nanoparticles in the AFSDed-4h-SST sample.

[15] is applied:

$$D^n - D_0^n = ct \quad (1)$$

where D_0 is the initial grain size, D is the final grain size, n is the grain growth exponent, t is the dwelling time, and c is the grain growth constant that describes the rate of grain growth. For the grain growth in this work, the initial grain size D_0 and the final grain size D were measured from the EBSD maps, and the time t was recorded. The grain growth exponent n depends on the material and sometimes also on the temperature. The grain growth exponent n of the feedstock can be extracted from Fig. 6a by analysing the relationship between ln(dD/dt) and lnD [36,37], which is determined to be ~2.5. This value should also apply to the AFSDed material, which was heat-treated at the same temperature. Thus the relationship between $D^n - D_0^n$ and t can be plotted. The slope from Fig. 6b is the grain growth rate c, according to Eq. (1). The grain growth rate c of the feedstock is calculated to be

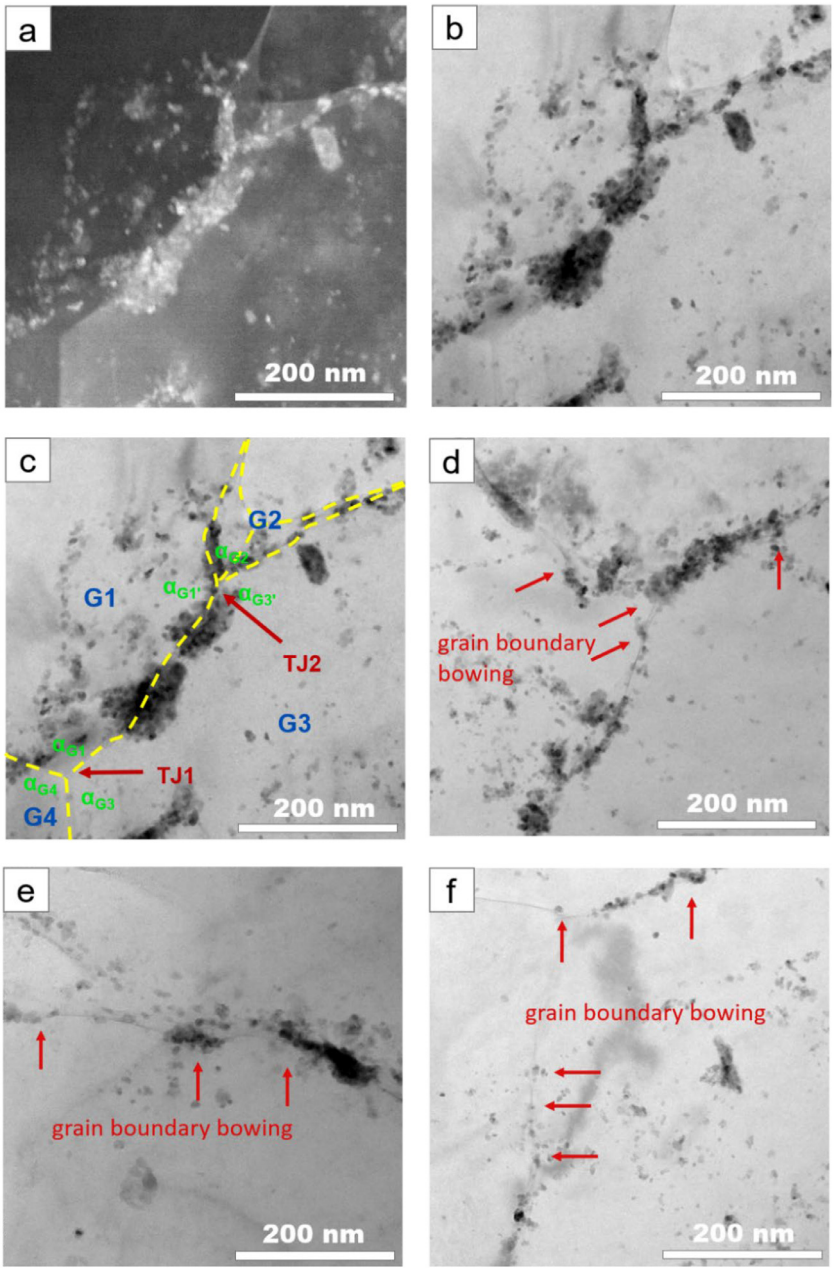

Fig. 4. S/TEM images of a region in AFSDed-4h-SST (a) HAADF image, (b) BF image, (c) BF image with a sketch of grain boundaries. (d-f) BF images of other regions with grain boundary bowing, indicated by red arrows.

200 $\mu m^{2.5}$/min. For the AFSDed sample, as $D \approx D_0$, the value of the grain growth constant c is nearly 0, indicating complete grain growth stagnation. This result statistically demonstrates the extraordinary thermal stability of the grain structure in the AFSDed material.

4.2. Driving force and retarding force of the grain growth

To understand the significant difference in the grain growth rate for the material with the same chemical composition, it is essential to analyse the driving and retarding forces in detail. Two major sources of the driving force for grain boundary migration are the stored deformation energy and the stored surface energy in the grain boundaries. The stored deformation energy promotes the grain boundary migration by recrystallisation. Grain orientation spread (GOS) maps of the AFSDed sample and the feedstock are shown in Fig. 7. Grains with a GOS value smaller than 2° are regarded as recrystallised grains. The recrystallisation fraction measured from the map was 87% for the AFSDed sample and 93% for the feedstock. Both samples exhibited a highly recrystallised structure and the contribution of stored deformation energy should be similar and negligible. The surface energy stored in the grain boundaries drives the system to reduce the grain boundary area through grain growth, which is driven by the boundary curvature and thus closely related to the grain size. The

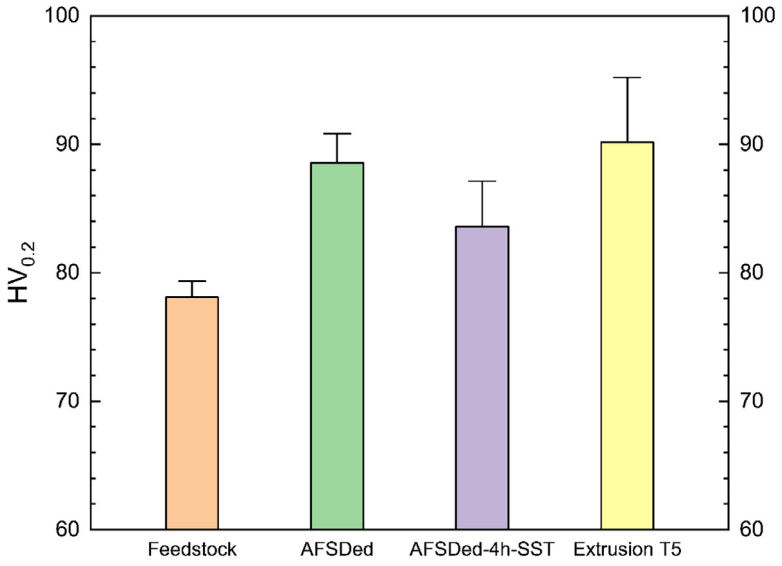

Fig. 5. Vickers hardness test results of Elektron 43 in different conditions.

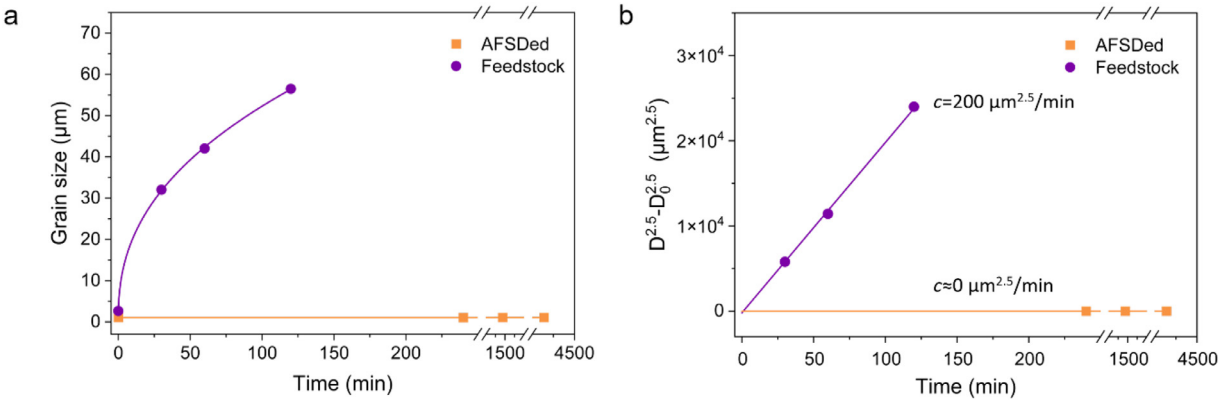

Fig. 6. (a) Grain size change with time, (b) Plot of $D^{2.5} - D_0^{2.5}$ against time.

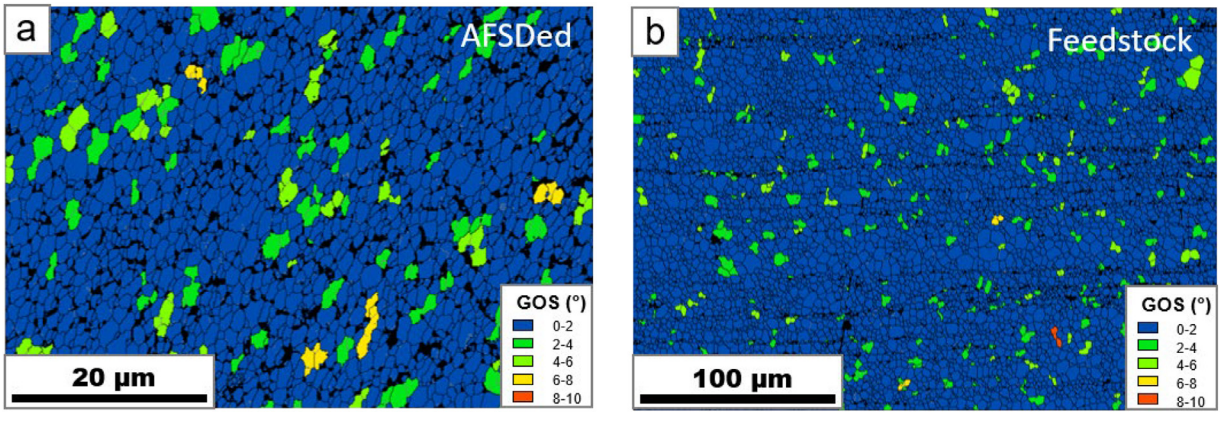

Fig. 7. GOS maps of (a) AFSDed sample; (b) feedstock material.

driving force originates from the curvature is described as [34]:

$$P_c = \frac{4\gamma}{D} \tag{2}$$

where P_c is the driving force by grain boundary curvature, γ is the grain boundary energy, D is the grain size. The grain boundary energy γ can be affected by various factors such as grain boundary misorientation, but both samples are expected to have the similar grain boundary energy γ ~0.4 J/m^2 [34]. Consequently, the driving force provided by the grain boundary curvature in the AFSDed sample should be nearly twice that in the feedstock, since the average grain

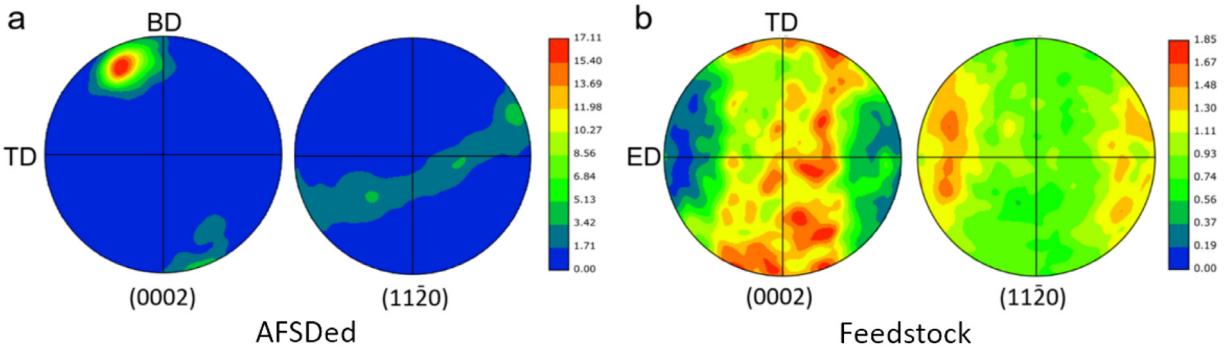

Fig. 8. Pole figures of (a) AFSDed sample, (b) feedstock material.

size in the AFSDed sample is only about half of that in the feedstock. In addition to the boundary curvature, texture components sometimes play an important role in boundary mobility [15,38]. In Mg alloys, it has been reported that grains with (0001) <11$\bar{2}$0> texture components, which is the case for the AFSDed sample, as shown in the Fig. 8, tend to grow quicker than other grains [39]. However, at elevated temperatures (e.g. 525 °C in this work), such preferential grain growth is believed to be significantly extenuated [39]. In summary, the overall driving force for grain growth in the AFSDed material is expected to be higher than that in the feedstock.

However, the experiment results indicated rapid grain growth in the feedstock but grain growth stagnation in the AFSDed material. This suggests that there must be strong retarding force in the AFSDed material. There are two major microstructural factors retarding the grain boundary migration, grain boundary solute segregation [40,41] and particles [15,16,41,42]. The solute atoms segregating at grain boundaries affects the grain growth behaviour from two perspectives. Alloying atoms segregated at grain boundaries can decrease the driving force by decreasing the boundary energy. Additionally, segregated atoms exert a retarding force by solute drag [15]. The effectiveness of the grain boundary segregation is affected by several factors, such as concentration and temperature. The solute drag effect has been reported to become negligible at elevated temperatures [34,35,43], making its contribution in this study insignificant. Particles can also effectively retard grain growth by pinning the grain boundary and triple junction movement [2,44]. Despite the effectiveness of particle pinning, the SST temperature is expected to promote the dissolution of Mg-Y, Mg-RE, or Mg-Y-RE phase (e.g. the $Mg_{41}RE_5$ phase in Fig. 3a), into the matrix, rendering most of the particles ineffective in the restriction of grain growth [34], as observed in the feedstock material. There were small amounts of residual large particles which are believed to be large oxides and rare earth hydrides, but they did not exhibit effective pinning effects. In contrast, in the AFSDed-4h-SST sample, nanoparticles did not show any statistically meaningful change in size, distribution, and density after a long period of holding at 525 °C, exhibiting exceptional thermal stability. There is no doubt that these nanoparticles play a fundamental role in grain growth stagnation.

4.3. Evolution of nanoparticles

These nanoparticles were not observed in the feedstock and therefore formed in-situ during the AFSD process. The high temperature generated by friction and surface exposure to air enables the rapid formation of oxides. Considering the relatively low temperature (i.e. solid state processing) and short exposure time during the AFSD process, the formed oxide particles remained the nano-size. In addition, the mechanical stirring generates material flow, re-distributing particles in the material [45]. The 'teardrop' structures on the tool surface assisted material flow along the building direction. This allows oxides to be distributed throughout the deposited layer instead of staying on the surface layer. Regarding the chemical composition of oxide particles, Zhao et al. [46] pointed out that the very initial oxidation stage involves the formation of zirconium oxides, magnesium oxides, and yttrium oxides, and later only yttrium oxides remain. Soderlind et al. also [47] suggested that magnesium oxide would transform to yttrium oxide at elevated temperatures. Such evolution is consistent with the Gibbs free energy of the formation of the alloying element oxides [48]. Y has the lowest Gibbs free energy when forming oxides and thus yttrium oxide is more thermodynamically stable, compared to other alloying elements and Mg. Although there is lack of direct observation of the oxide evolution in the AFSD process, based on EDS results in this work, oxidation process by other researchers, and thermodynamic data, the oxide formation process during AFSD and the following SST can be summarised. At the early stage of oxide formation, there is mainly Y_2O_3, yet small amount of other phases will also form, including ZrO_2, MgO, possibly Nd_2O_3, and Gd_2O_3. There is also possibly ternary oxide, such as $Y_2Zr_2O_7$. In the following heat treatment process, alloying elements in the less stable oxides (e.g. Mg and Zr) will be substituted by other elements which can form more stable oxides (e.g. Y). In other words, the process that less stable oxides transform to more stable oxides will be activated during the following SST. Considering the negligible solubility of O in metallic

materials, further formation of new oxide nuclei or change in oxide fraction is not possible during the following heat treatment.

4.4. Effects of nanoparticles

The interaction between nanoparticles-grain boundaries and nanoparticles-triple junctions was observed in AFSD-4h-SSTed sample as shown in Fig. 4. The significant grain boundary bowing indicates that the nanoparticles contribute to the pinning of grain boundary movement during the SST, which is usually referred to as Zener pinning [15]. The driving force of grain growth and Zener pinning force is usually expressed as [15,34]:

$$P_z = \frac{3f\gamma}{2r} \tag{3}$$

$$P_{z'} = \frac{Df\gamma}{4r^2} \tag{4}$$

where f is the volume fraction of particles, r is the radius of particles, P_z is the Zener pressure when particles are distributed randomly, $P_{z'}$ is the Zener pressure when particles are fully distributed at grain boundaries. It is obvious that for Zener pining, in addition to the grain boundary energy γ, the pinning force is also influenced by the volume fraction and size of the particles. A larger volume fraction of particles and smaller particle size can generate stronger Zener pinning force. The particle distribution also affects the effectiveness of Zener pining, and the grain size needs to be considered for the situation when particles accumulate at grain boundaries. There is a limiting grain size for Zener pining when the driving force is equal to the Zener pinning force, and it can be calculated as [15]:

$$D_z = \frac{8r}{3f} \tag{5}$$

$$D_{z'} = \frac{4r}{\sqrt{f}} \tag{6}$$

where D_z is the Zener limiting grain size when $P_z = P_c$, $D_{z'}$ is the Zener limiting grain size when $P_{z'} = P_c$, corresponding to the two different particle distribution situations in the AFSDed sample, D was measured to be around 1.05 μm, f and r was calculated by using ImageJ to be about 0.07 and 32 nm, respectively. It is clear that $P_{z'}$ is larger than P_z in this situation. This means in the AFSDed sample, the preferential distribution of nanoparticles at grain boundaries provides stronger pinning effects, compared to the random distribution, and the equilibrium grain size should fall between D_z and $D_{z'}$. D_z was calculated to be about 1.37 μm and $D_{z'}$ was calculated to be about 0.48 μm. This is consistent with the measured grain size of 1.05 μm, verifying the role of Zener pining and the effectiveness of grain boundary accumulation.

For triple junction sites, there should be an angle of 120° when three grains meet at the vertex, to achieve the balanced state. This is often expressed as the following equation [15]:

$$\frac{\gamma_{12}}{\sin\alpha_3} = \frac{\gamma_{13}}{\sin\alpha_2} = \frac{\gamma_{23}}{\sin\alpha_1} \tag{7}$$

where α_1, α_2, α_3 are the corresponding angles opposite to the boundaries. This is the case for the TJ1 in Fig. 4, where no nanoparticles are present. The boundary tension forces are similar and the three angles α_{G1}, α_{G3}, α_{G4} are around 120° For TJ2 where G1, G2, and G3 meet, the angles $\alpha_{G1'}$, α_{G2}, $\alpha_{G3'}$ are away from 120° This is because the nanoparticles provide an extra restraining effect, bringing it to a balanced state without achieving angles equal to 120°

In addition to the strong pinning effects on grain boundary movement, the nanoparticles also contribute to the hardness increase. The hardness of the AFSDed sample is ~10 HV higher than that of the feedstock. The hardness contribution from grain boundary strengthening can be calculated using the following equation:

$$\Delta HV_{GB} = Ckd^{-1/2} \tag{8}$$

where C is the yield strength-micro hardness proportional constant ~0.3 HV/MPa, and k is Hall-Petch constant for Mg-Y-RE alloys ~40.7MPa·μm$^{1/2}$ [49]. Considering the minor grain size difference between 1.05 μm and 2.64 μm in two samples, ΔHV_{GB} difference can be calculated ~4 HV, which is smaller than the overall difference ~10 HV. Oxide nanoparticles are believed to provide extra strengthening effects in addition to the grain boundary strengthening. While systematic investigations of the effects of thermally stable nanoparticles on grain boundaries in magnesium alloys remain in the initial stages, it is well known that in ODS alloys, dispersed oxides improve mechanical properties at elevated temperatures, inhibiting the dissolution of strengthening precipitates, grain growth, grain boundary sliding, and grain rotation [50]. The influence of oxide nanoparticles on grain growth has been discussed in this work and other potential effects will be investigated in the future.

5. Conclusions

It is the first time that complete grain growth stagnation has been observed at 525 °C (0.87 T_m) for 72 h in an Elektron 43 Mg alloy with UFG structure fabricated by AFSD. The microstructural evolution of the AFSDed Mg alloy and the feedstock material was investigated, leading to the following conclusions:

(1) In the AFSDed Elektron 43, two major second phases were identified: large $Mg_{41}RE_5$ particles around 1 μm, and dense nanoparticles mainly composed of Y and O, either in the form of single crystals or agglomerations.
(2) The nanoparticles were not present in the feedstock but formed in-situ during the AFSD process due to the elevated temperature. They were redistributed throughout the deposited layer by the friction stirring, instead of staying on the surface.
(3) After 4 h SST, the $Mg_{41}RE_5$ phases in the AFSDed Elektron 43 were fully dissolved into the matrix, whilst the nanoparticles remained unchanged, showing strong interaction with grain boundaries and triples junctions (Zener pinning).

(4) The grain growth stagnation at 525 °C is attributed to the long-lasting and strong Zener pinning effects by oxide nanoparticles. This is due to several features of nanoparticles including high thermal stability, high volume fraction, small size, and preferential distribution along grain boundaries.

Declaration of competing interest

The authors declare that they have no known competing financial interests or personal relationships that could have appeared to influence the work reported in this paper.

CRediT authorship contribution statement

Xingjian Zhao: Writing – review & editing, Writing – original draft, Validation, Methodology, Investigation. **Daniel Olden:** Validation, Methodology, Investigation. **Brady Williams:** Resources, Methodology, Conceptualization. **Abhishek Pariyar:** Writing – review & editing, Methodology. **Dalong Zhang:** Writing – review & editing. **Matthew Murphy:** Resources, Methodology. **Philippa Reed:** Writing – review & editing, Supervision. **Paul Allison:** Writing – review & editing, Resources, Methodology, Conceptualization. **Brian Jordon:** Writing – review & editing, Resources, Methodology, Conceptualization. **Jiahui Qi:** Investigation. **W. Mark Rainforth:** Writing – review & editing, Supervision. **Dikai Guan:** Writing – review & editing, Writing – original draft, Supervision, Resources, Project administration, Funding acquisition, Conceptualization.

Acknowledgement

This work was supported by the UKRI Future Leaders Fellowship, [MR/T019123/2]. We acknowledge the TEM access supported by Kaiple Electron Microscope Centre. We would like to acknowledge the support of the Henry Royce Institute for advanced materials for DG through the Researcher Equipment Access Scheme enabling access to JEOL F200 TEM facilities at The Sorby Centre for Electron Microscopy, [EP/R00661X/1 & EP/P02470X/1].

References

[1] S. Liang, X. Liu, S. Jiang, H. Zhu, W. Li, L. Liu, X. Liu, Y. Wu, X. Zhang, H. Wang, Z. Lu, J. Mater. Sci. Technol. 181 (2024) 220–230, doi:10.1016/j.jmst.2023.08.069.

[2] Q. Zhang, W. Wang, Q. Yuan, Z. Wang, Z. Zhang, G. Xu, Met. Mater. Int. 29 (7) (2022) 2018–2027, doi:10.1007/s12540-022-01352-z.

[3] J.R. Croteau, J.-G. Jung, S.A. Whalen, J. Darsell, A. Mello, D. Holstine, K. Lay, M. Hansen, D.C. Dunand, N.Q. Vo, Scr. Mater. 186 (2020) 326–330, doi:10.1016/j.scriptamat.2020.05.051.

[4] A. Hanna, H. Azzeddine, Y. Huang, D. Bradai, J.M. Cabrera, T.G. Langdon, Mater. Charact. 151 (2019) 519–529, doi:10.1016/j.matchar.2019.03.040.

[5] J. Stráská, M. Janeček, J. Čížek, J. Stráský, B. Hadzima, Mater. Charact. 94 (2014) 69–79, doi:10.1016/j.matchar.2014.05.013.

[6] V. Segal, Materials (Basel) 11 (7) (2018) 1175, doi:10.3390/ma11071175.

[7] A. Azushima, R. Kopp, A. Korhonen, D.Y. Yang, F. Micari, G.D. Lahoti, P. Groche, J. Yanagimoto, N. Tsuji, A. Rosochowski, A. Yanagida, CIRP. Ann. Manuf. Technol. 57 (2) (2008) 716–735, doi:10.1016/j.cirp.2008.09.005.

[8] D.X. Liu, X. Pang, D.L. Li, C.G. Guo, J. Wongsa-Ngam, T.G. Langdon, M.A. Meyers, Adv. Eng. Mater. 19 (3) (2017) 1600698, doi:10.1016/j.cirp.2008.09.005.

[9] P. Seenuvasaperumal, K. Doi, D.A. Basha, A. Singh, A. Elayaperumal, K. Tsuchiya, Mater. Lett. 227 (2018) 194–198, doi:10.1016/j.matlet.2018.05.076.

[10] P. Minárik, J. Veselý, R. Král, J. Bohlen, J. Kubásek, M. Janeček, J. Stráská, Mater. Sci. Eng. A. Struct. Mater. 708 (2017) 193–198, doi:10.1016/j.msea.2017.09.106.

[11] H. Utsunomiya, K.-i. Izumi, T. Sakai, T. Mukai, J. Phys. Conf. Ser. 165 (2009), doi:10.1088/1742-6596/165/1/012011.

[12] C. Wang, M. Sun, F. Zheng, L. Peng, W. Ding, J. Magnes. Alloy. 2 (3) (2014) 239–244, doi:10.1016/j.jma.2014.09.001.

[13] C. Chang, X. Du, J. Huang, Scr. Mater. 59 (3) (2008) 356–359, doi:10.1016/j.scriptamat.2008.04.003.

[14] H. Zhou, N. Deng, H. Zhang, C. Zhang, Y. Lu, K. Gao, G. Wang, S. Sun, X. Wang, J. Sci. Eng. 47 (7) (2021) 8373–8383, doi:10.1007/s13369-021-06284-1.

[15] J. Humphreys, G.S. Rohrer, A. Rollett, 2017.

[16] X. Bai, H. Xie, X. Zhang, D. Zhao, X. Rong, S. Jin, E. Liu, N. Zhao, C. He, Nat. Mater. 23 (6) (2024) 747–754, doi:10.1038/s41563-024-01884-2.

[17] K. Fekete, D. Drozdenko, P. Cejpek, P. Dobroň, J. Veselý, M. Yamasaki, Y. Kawamura, Mater. Charact. 183 (2022), doi:10.1016/j.matchar.2021.111618.

[18] P. Minárik, J. Veselý, J. Čížek, M. Zemková, T. Vlasák, T. Krajňák, J. Kubásek, R. Král, D. Hofman, J. Stráská, Mater. Charact. 140 (2018) 207–216, doi:10.1016/j.matchar.2018.04.006.

[19] O.G. Rivera, P.G. Allison, J.B. Jordon, O.L. Rodriguez, L.N. Brewer, Z. McClelland, W.R. Whittington, D. Francis, J. Su, R.L. Martens, N. Hardwick, Mater. Sci. Eng. A. Struct. Mater. 694 (2017) 1–9, doi:10.1016/j.msea.2017.03.105.

[20] H.Z. Yu, M.E. Jones, G.W. Brady, R.J. Griffiths, D. Garcia, H.A. Rauch, C.D. Cox, N. Hardwick, Scr. Mater. 153 (2018) 122–130, doi:10.1016/j.scriptamat.2018.03.025.

[21] H.Z. Yu, R.S. Mishra, Mater. Res. Lett. 9 (2) (2020) 71–83, doi:10.1080/21663831.2020.1847211.

[22] B.E.T. Roper, C.M. Roper, H.M. Rao, L.N. Brewer, V.K. Vasudevan, N. Zhu, J.B. Jordon, P.G. Allison, Metallogr. Microstruc. 13 (1) (2024) 174–180, doi:10.1007/s13632-024-01043-8.

[23] M. Gor, M. Barnett, D. Fabijanic, P.P. Bhattacharjee, Addit. Manuf. Lett. 9 (2024) 100204, doi:10.1016/j.addlet.2024.100204.

[24] D. Garcia, W.D. Hartley, H.A. Rauch, R.J. Griffiths, R. Wang, Z.J. Kong, Y. Zhu, H.Z. Yu, Addit. Manuf. 34 (2020), doi:10.1016/j.addma.2020.101386.

[25] M.E.J. Perry, H.A. Rauch, R.J. Griffiths, D. Garcia, J.M. Sietins, Y. Zhu, Y. Zhu, H.Z. Yu, Materialia (Oxf) 18 (2021) 101159, doi:10.1016/j.mtla.2021.101159.

[26] A. Pariyar, E. Yasa, A. Sharman, C.S. Perugu, L. Yuan, J. Hughes, D. Guan, Mater. Des. 245 (2024) 113238, doi:10.1016/j.matdes.2024.113238.

[27] M.B. Williams, T.W. Robinson, C.J. Williamson, R.P. Kinser, N.A. Ashmore, P.G. Allison, J.B. Jordon, Metals (Basel) 11 (11) (2021) 1739, doi:10.3390/met11111739.

[28] S.S. Joshi, S.M. Patil, S. Mazumder, S. Sharma, D.A. Riley, S. Dowden, R. Banerjee, N.B. Dahotre, J. Magnes. Alloy. 10 (9) (2022) 2404–2420, doi:10.1016/j.jma.2022.03.011.

[29] S. Sharma, K.V. Mani Krishna, M. Radhakrishnan, M.V. Pantawane, S.M. Patil, S.S. Joshi, R. Banerjee, N.B. Dahotre, Mater. Des. 224 (2022) 111412, doi:10.1016/j.matdes.2022.111412.

[30] S.S. Joshi, S. Sharma, M. Radhakrishnan, M.V. Pantawane, S.M. Patil, Y. Jin, T. Yang, D.A. Riley, R. Banerjee, N.B. Dahotre, Sci. Rep. 12 (1) (2022) 13234, doi:10.1038/s41598-022-17566-5.

[31] T. Luo, W. Tang, R. Wang, S. Wang, L. Xiao, X. Yang, Mater. Lett. 340 (2023) 134164, doi:10.1016/j.matlet.2023.134164.
[32] A. Salandari-Rabori, A. Zarei-Hanzaki, S. Asqardoust, H.R. Abedi, T. Krajňák, P. Minárik, J. Veselý, Mater. Lett. 337 (2023) 134006, doi:10.1016/j.matlet.2023.134006.
[33] F. Bar, L. Berger, L. Jauer, G. Kurtuldu, R. Schaublin, J.H. Schleifenbaum, J.F. Loffler, Acta. Biomater. 98 (2019) 36–49, doi:10.1016/j.actbio.2019.05.056.
[34] D. Guan, W.M. Rainforth, J. Gao, L. Ma, B. Wynne, Acta. Mater. 145 (2018) 399–412, doi:10.1016/j.actamat.2017.12.019.
[35] Q. Wang, H. Zhai, H. Xia, L. Liu, J. He, D. Xia, H. Yang, B. Jiang, Acta Metall. Sin. (Engl. Lett.) 35 (11) (2022) 1793–1811, doi:10.1007/s40195-022-01395-6.
[36] X. Wang, L. Hu, K. Liu, Y. Zhang, J. Alloys. Compd. 527 (2012) 193–196, doi:10.1016/j.jallcom.2012.03.006.
[37] Q. Miao, L. Hu, X. Wang, E. Wang, J. Alloys. Compd. 493 (1–2) (2010) 87–90, doi:10.1016/j.jallcom.2009.12.049.
[38] X. Zeng, H. Yi, Z. Zeng, L. Yuan, S. Yi, J. Gao, M. Rainforth, D. Guan, J. Mater. Sci. Technol. 197 (2024) 149–159, doi:10.1016/j.jmst.2024.02.013.
[39] R. Pei, S. Korte-Kerzel, T. Al-Samman, J. Mater. Sci. Technol. 50 (2020) 257–270, doi:10.1016/j.jmst.2020.01.014.
[40] R. Pei, Y. Zhao, M. Zubair, S. Yi, T. Al-Samman, J. Magnes. Alloy. 11 (7) (2023) 2312–2325, doi:10.1016/j.jma.2023.06.008.
[41] Z.-Y. Meng, C. Wang, Z.-M. Hua, M. Zha, H.-Y. Wang, Mater. Res. Lett. 10 (12) (2022) 797–804, doi:10.1080/21663831.2022.2106797.
[42] J. Gao, S. Jiang, H. Zhang, Y. Huang, D. Guan, Y. Xu, S. Guan, L.A. Bendersky, A.V. Davydov, Y. Wu, H. Zhu, Y. Wang, Z. Lu, W.M. Rainforth, Nat 590 (7845) (2021) 262–267, doi:10.1038/s41586-021-03246-3.
[43] D. Guan, W.M. Rainforth, J. Gao, J. Sharp, B. Wynne, L. Ma, Acta. Mater. 135 (2017) 14–24, doi:10.1016/j.actamat.2017.06.015.
[44] W. Sun, Y. He, X. Qiao, X. Zhao, H. Chen, N. Gao, M.J. Starink, M. Zheng, J. Magnes. Alloy. 11 (12) (2023) 4589–4602, doi:10.1016/j.jma.2022.04.003.
[45] X. Zhao, X. Zeng, L. Yuan, J. Gandra, Q. Hayat, M. Bai, W.M. Rainforth, D. Guan, Scr. Mater. 227 (2023) 115301, doi:10.1016/j.scriptamat.2023.115301.
[46] X. Zhao, Z. Ning, Z. Li, W. Zou, B. Li, K. He, F. Cao, J. Sun, A.A. Luo, J. Mater. Sci. 53 (15) (2018) 11091–11103, doi:10.1007/s10853-018-2271-y.
[47] J. Soderlind, M. Cihova, R. Schaublin, S. Risbud, J.F. Loffler, Acta. Biomater. 98 (2019) 67–80, doi:10.1016/j.actbio.2019.06.045.
[48] I. Barin, 1995.
[49] Y. Li, C. Qu, J. Wang, R. Xu, J. Alloys. Compd. 813 (2020) 152123, doi:10.1016/j.jallcom.2019.152123.
[50] R. Gao, T. Zhang, X.P. Wang, Q.F. Fang, C.S. Liu, J. Nucl. Mater. 444 (1–3) (2014) 462–468, doi:10.1016/j.jnucmat.2013.10.038.